

Geometrically stabilized skyrmionic vortex in FeGe tetrahedral nanoparticles

Kodai Niitsu[®]^{1,2,8}, Yizhou Liu^{1,8}, Alexander C. Booth[®]³, Xiuzhen Yu[®]¹, Nitish Mathur⁴, Matthew J. Stolt⁴, Daisuke Shindo¹, Song Jin[®]⁴, Jiadong Zang[®]^{3,5}, Naoto Nagaosa^{1,6} and Yoshinori Tokura[®]^{1,6,7}

The concept of topology has dramatically expanded the research landscape of magnetism, leading to the discovery of numerous magnetic textures with intriguing topological properties. A magnetic skyrmion is an emergent topological magnetic texture with a string-like structure in three dimensions and a disk-like structure in one and two dimensions. Skyrmions in zero dimensions have remained elusive due to challenges from many competing orders. Here, by combining electron holography and micromagnetic simulations, we uncover the real-space magnetic configurations of a skyrmionic vortex structure confined in a B20-type FeGe tetrahedral nanoparticle. An isolated skyrmionic vortex forms at the ground state and this texture shows excellent robustness against temperature without applying a magnetic field. Our findings shed light on zero-dimensional geometrical confinement as a route to engineer and manipulate individual skyrmionic metastructures.

agnetic structures in confined geometries have become a versatile platform for realizing the vast potential of these structures in diverse applications. In particular, the engineering of magnetic structures has been intensively studied in two-dimensional (2D) and one-dimensional (1D) ferromagnets, wherein the magnetic domain structures accommodate their own physical and microstructural features into reduced dimensions^{1,2}. In contrast, although confined in zero dimensions (0D), that is, in nanoparticles, sophisticated three-dimensional (3D) magnetic structures can still develop under appropriate conditions. Although visualizing spatial magnetic configurations inside 1D nanorods^{3–8} and 2D thin foils^{9–11} is now possible using electron^{3–5,9,10}, neutron⁶ and X-ray^{7,8,11} sources, such visualization inside an isolated 0D nanoparticle remains challenging ^{12–14}.

Meanwhile, the Dzyaloshinskii-Moriya (DM) interaction has provided new opportunities to tailor topological states in magnetic systems. One of the most remarkable advances has been the discovery of magnetic skyrmions, which are topological swirling spin configurations that are typically stabilized in material systems with broken inversion symmetry^{15–17}. Their topological particle-like nature in two dimensions and the extremely low critical current density needed to drive their motion have potential for manipulating individual skyrmions in future spintronic devices^{18–24}. To enable their practical application, methods to isolate a skyrmion from the skyrmion lattice or other competing magnetic states have been intensively explored²⁵⁻²⁹. One of the most promising methods for skyrmion isolation is geometrical confinement in low dimensions. Skyrmions are stabilized in 2D with an extended phase region with respect to the magnetic field and temperature³⁰. Geometrical confinement in 2D allows the emergence of a limited number of skyrmions^{31,32} or even a single zero-field target skyrmion^{33–35}. Similarly, 1D nanorods can confine a skyrmion chain, which is expected to be a building block for skyrmion racetrack memory^{22,26-29,36,37}. In this sense, nanoparticles with strong geometrical confinement are expected to be a promising host for isolated skyrmions. However, in nanoparticles with specific symmetries, the interplay of bulk chiral spin interactions and geometrical symmetry invokes chiral geometrical frustration, especially when the geometrical size of the nanoparticle is comparable to the helimagnetic wavelength. This new class of frustration may provide an additional degree of freedom to realize novel magnetic structures. Therefore, the visualization of emergent magnetic configurations in a single nanoparticle could provide novel insight into the role of geometrical confinement as well as technical advancements in real-space magnetic imaging.

In this study we developed and performed multiangle electron holography (EH) on chemically synthesized isolated tetrahedral particles of B20-type FeGe to reveal their internal 3D magnetic configurations. Integrating EH observations and micromagnetic simulations uncovered real-space magnetic configurations that dramatically change with particle size. Although particles with a size of several hundred nanometres can reasonably host the helimagnetic ground state, nanoparticles with sizes comparable to the helical wavelength (~70 nm for FeGe (ref. ³⁰)) can lead to the emergence of a novel skyrmionic vortex structure, revealing the topological nature of a skyrmion string. This texture shows excellent robustness against temperature without applying a magnetic field; thus, a zero-field skyrmionic ground state is realized for a certain size range of tetrahedral particles.

Morphology and crystallography of the synthesized particles. Scanning electron microscopy (SEM) images and an X-ray diffraction (XRD) pattern of the products synthesized using a chemical vapour deposition method are presented in Fig. 1a,b. The products were composed of various morphologies, such as tetrahedra,

¹RIKEN Center for Emergent Matter Science (CEMS), Wako, Japan. ²Department of Materials Science and Engineering, Kyoto University, Kyoto, Japan. ³Department of Physics and Astronomy, University of New Hampshire, Durham, NH, USA. ⁴Department of Chemistry, University of Wisconsin-Madison, Madison, WI, USA. ⁵Materials Science Program, University of New Hampshire, Durham, NH, USA. ⁶Department of Applied Physics, University of Tokyo, Tokyo, Japan. ⁷Tokyo College, University of Tokyo, Tokyo, Japan. ⁸These authors contributed equally: Kodai Niitsu, Yizhou Liu. [⊠]e-mail: NIITSU.Kodai@nims.go.jp; Jiadong.Zang@unh.edu

ARTICLES NATURE MATERIALS

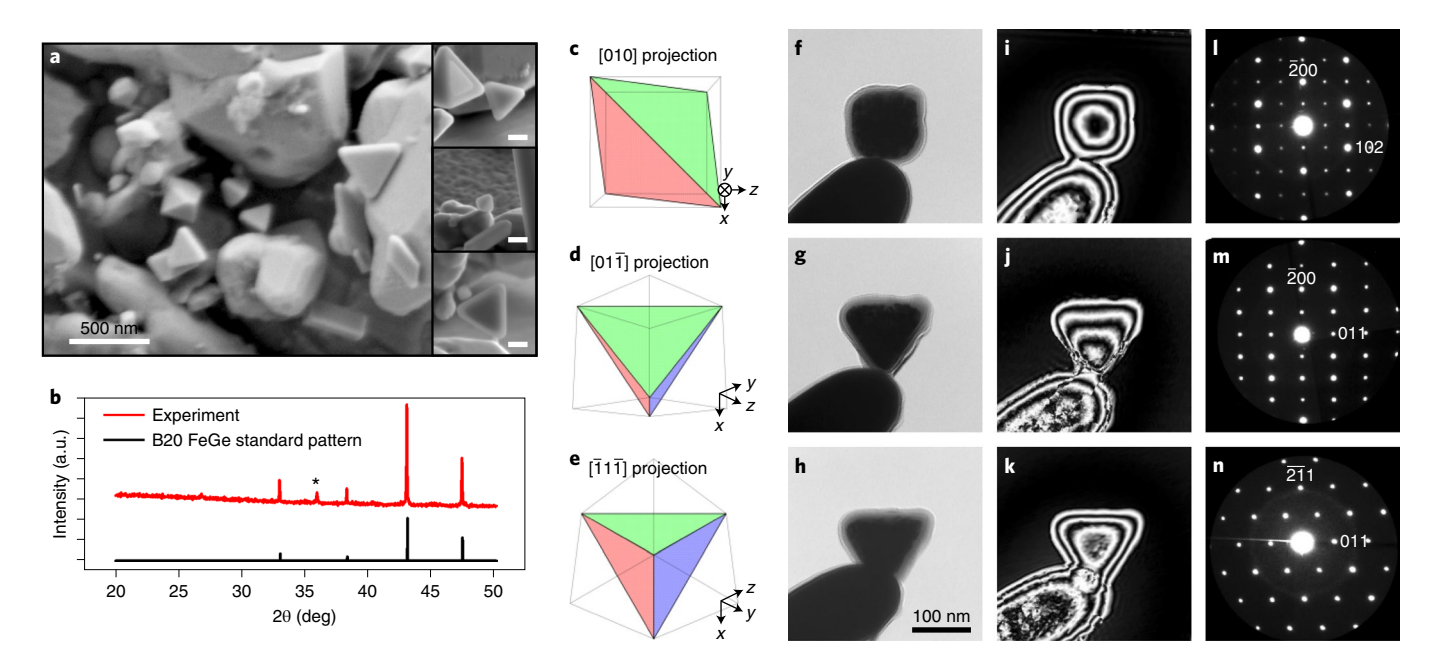


Fig. 1 Morphology and crystallography of FeGe tetrahedral particles. **a**, SEM images of the synthesized FeGe products. The right column presents magnified views of the well-faceted tetrahedral particles. Scale bars (right column), 200 nm. **b**, XRD pattern obtained from the products and reference pattern for the B20 FeGe cubic crystal structure (JCPDS PDF number 65-6357). The peak marked by the asterisk corresponds to the (120) peak of the hexagonal FeGe crystal structure of the faceted nanowires. **c-e**, Schematics of a tetrahedron projected along the [010] (**c**), $\begin{bmatrix} 011 \end{bmatrix}$ (**d**) and $\begin{bmatrix} \overline{1}11 \end{bmatrix}$ (**e**) directions. **f-h**, Corresponding TEM images. **i-k**, Corresponding phase (φ) maps taken at 293 K displayed in the form of cos φ . **I-n**, Corresponding nanobeam diffraction patterns indexed with the [010], $\begin{bmatrix} 01\overline{1} \end{bmatrix}$ and $\begin{bmatrix} \overline{1}1\overline{1} \end{bmatrix}$ zone axes.

octahedra and rounded/faceted nanowires. Most were indexed as the B20 cubic crystal structure of FeGe, except for one peak in the XRD pattern assigned to the hexagonal FeGe crystal structure of well-faceted nanowires³⁶. The crystallography and crystallinity of highly symmetric tetrahedral particles with various sizes from approximately 100 nm to over 500 nm (Fig. 1a, right column) were identified using conventional transmission electron microscopy (TEM) observations, multiangle EH observations and the nanobeam diffraction technique (Fig. 1c-n); these examinations were performed at 293 K, which is above the magnetic ordering temperature (T_c) of 280 K³⁰. According to conventional TEM observations (Fig. 1f-h), which were obtained from the three representative projections in Fig. 1c-e, the particle consisted of a highly crystalline body with high tetrahedral symmetry and amorphous surfaces less than ~10 nm thick; the detailed structural and chemical properties of the amorphous region are given in Supplementary Note 1. In the corresponding phase images (Fig. 1i-k), because the phase undulations in the paramagnetic state refer to the change in the mean electrostatic potential integrated along the beam trajectory, which is qualitatively identical to the variations in thickness, the different phase variations (Fig. 1j,k) enable the two projections (Fig. 1g,h) to be distinguished. A systematic set of diffraction patterns of the particles (Fig. 11-n) was unambiguously assigned to the B20 cubic structure with tetrahedral facets in the {111} planes. The crystallography was consistent with the XRD pattern for the synthesized products (Fig. 1b).

Multiangle EH observation of skyrmionic vortex. EH studies for visualizing magnetic textures were performed for the [010], $[01\overline{1}]$ and $[00\overline{1}]$ projections. The EH images represent the projections of the in-plane magnetic fluxes integrated along the beam trajectory (for the detailed acquisition protocol, see Methods and Supplementary Note 2). The most striking magnetization texture appears in a 145 nm tetrahedral particle (Fig. 2a) at 10 K, TEM images of which are presented in Fig. 2c-e. Systematic EH imaging

reveals a swirling in-plane magnetic flux along the [001] direction (Fig. 2f), a distorted swirling in-plane magnetic flux along the [011] direction (Fig. 2g) and an unconventional magnetic flux distribution along the [010] direction (Fig. 2h). Figure 2i-k shows the corresponding projections for the magnetic phase distribution calculated from micromagnetic simulations in a tetrahedral particle of the same size (see Methods and Supplementary Fig. 9 for details). The simulation captures the essential features of the observed magnetic texture well. The difference between the phase shift profiles along the lines in Fig. 2f,i is within reason (Fig. 2b). The phase shift in the simulation is underestimated because it does not account for the additional magnetic phase shift from the amorphous surface layer.

The simulated 3D magnetic configuration, herein named the skyrmionic vortex, is detailed in Fig. 2l-n and Supplementary Movies 1-4. Its non-triviality is indicated by the tube-like equi-spin surface. The equi-spin surface with the z component (along the [001] direction) of magnetization $S_z = 0$ forms a tube stretching along the [001] direction (Fig. 2m). The in-plane magnetic configurations also show that the tube in the skyrmionic vortex state forms in each cross section (Fig. 2m,n). The projected magnetic configuration along the $[00\bar{1}]$ direction (Fig. 21) resembles a vortex state with unity vorticity, in which in-plane magnetic moments rotate by an angle of 2π circulating around the centre. A unity vorticity state can be either a singularity, meron or skyrmion³⁸. The magnetic moments here are well defined everywhere; therefore, they cannot be a singularity. Furthermore, unlike meron states, the magnetic moments herein flip their z components from the centre to the periphery. The emergence of skyrmionic texture in this tetrahedron is further evidenced by the topological charge calculation, as detailed in Supplementary Note 4. In general, confined geometries have finite boundaries and the topological charge is no longer strictly integer-valued. By excluding the corner spin twists, the total topological charge enclosed by the dashed box in Fig. 21 has a fractional value of 0.93. Its slight deviation from 1 is mainly attributed to entanglement with corner spin twists at the boundary of the skyrmionic vortex.

NATURE MATERIALS ARTICLES

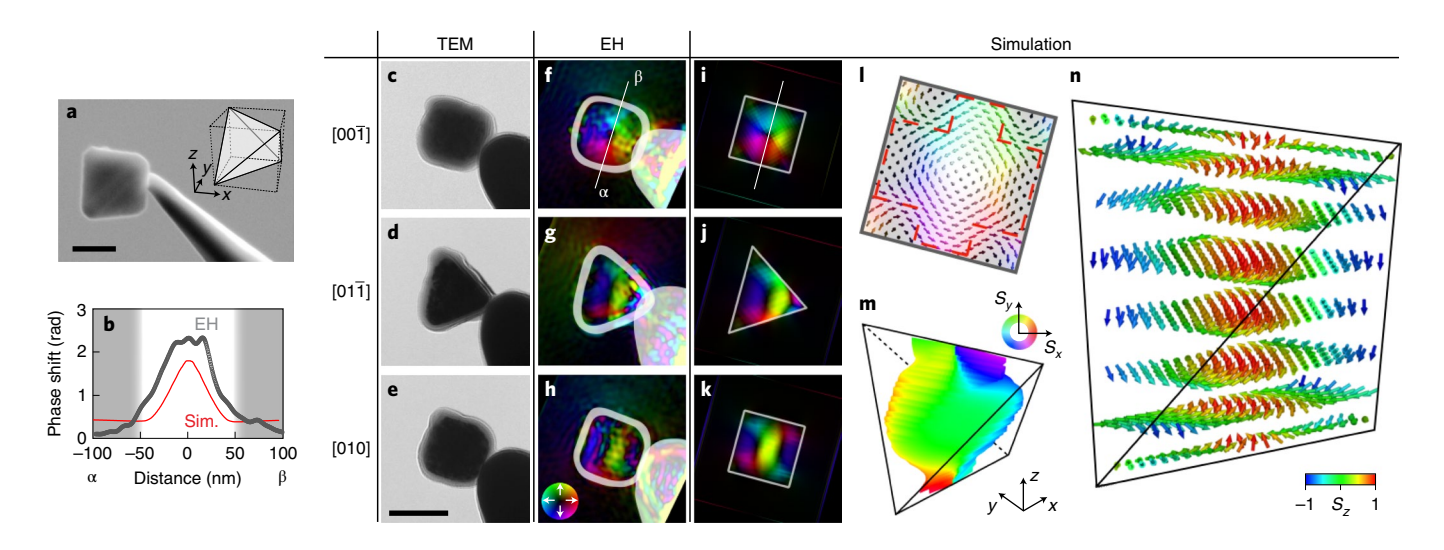


Fig. 2 | Skyrmionic vortex confined in a 145 nm FeGe tetrahedral particle. a, Scanning electron micrograph showing a nanoparticle supported on a probe. Inset: schematic of the crystallographic orientation. **b**, Phase-shift profiles along the lines in **f** and **i**. Sim., simulated. **c-e**, TEM images along the $\begin{bmatrix} 00\overline{1} \end{bmatrix}$ (**c**), $\begin{bmatrix} 01\overline{1} \end{bmatrix}$ (**d**) and $\begin{bmatrix} 010 \end{bmatrix}$ (**e**) directions. **f-h**, Observed in-plane magnetic flux distributions for the corresponding projections at 10 K. Masked regions cover the fringes and probe, where phase reconstruction or subtraction fails because of the abrupt change in the traversing thickness, poor visibility and/or slight deviation in the projection conditions at different temperatures. The colour wheel in **h** represents the direction and magnitude of the projected in-plane magnetic flux. **i-k**, Corresponding projections of the micromagnetic simulations. **I**, Magnetic configuration of **i** integrated along the $\begin{bmatrix} 00\overline{1} \end{bmatrix}$ direction. **m**, Equi-spin surface with the *z* component ($z = \begin{bmatrix} 001 \end{bmatrix}$) of magnetization $S_z = 0$. **n**, Magnetic configurations in cross-sectional planes normal to the *z* axis. Scale bars, 100 nm.

The skyrmionic vortex tube exhibits a richer structure than conventional skyrmion tubes³⁹. Although the core spins of the skyrmionic vortex pass through the [001] direction uniformly, the peripheral swirling pitch does not. A Bloch-like rotation with a wider pitch is present in the central cross section, a Néel-like rotation with a narrower pitch is emergent near the top and bottom, and mixed helicities are formed in between, altogether giving rise to the appearance of a potbelly-shaped equi-spin surface. In addition, a topological defect known as a fractional vortex⁴⁰ also forms on the edge due to chiral geometric frustration, that is, the interplay between the geometrical confinement of the tetrahedron and the bulk helimagnetic interaction (more details are given in the section Role of chiral geometric frustration). The two fractional vortices on the top and bottom edges are connected through a vertical line with spins pointing in the [001] direction (Fig. 2n) and facilitate the formation of the skyrmionic vortex tube.

With this portrait of the skyrmionic vortex, we can now readily interpret the observed and simulated projections (Fig. 2f-k) as follows: the [001] projections (Fig. 2f,i) are identical to the top view of this skyrmionic vortex, capturing the swirling contrasts. The [010] projections (Fig. 2h,k) are the side view, with the [001] polarity of the core colour-coded with yellow bars. The [011] projections (Fig. 2g,j) are intermediate projections, mixing the features of the top and side views and thus showing a distorted swirling texture. It is probable that a conventional magnetic vortex structure⁴¹ could yield similar projections. However, according to the comparative simulations for a vortex structure (Supplementary Fig. 21), the [010] projection of a vortex shows a remarkable contrast in a darker and narrower spine component compared with that of a skyrmionic vortex, which enables us to distinguish a skyrmionic vortex from a pure vortex. We therefore ruled out the possibility of a pure vortex state.

The variation of the observed and simulated in-plane magnetic flux projections for tetrahedral particles of various sizes is presented in Fig. 3. The series of EH observations of a particle further reduced in size (110 nm; Fig. 3a) still captures similar characteristics to those of the 145 nm particle except for the [010] projection. The

simulated results for this size again reveal the skyrmionic vortex with the in-plane winding and $[00\bar{1}]$ polarization reversal, as shown in Supplementary Fig. 14. The projections reproduce some essential features of the observations, supporting the emergence of a skyrmionic vortex. Excellent agreement between the observations and simulations is demonstrated for a particle with a size of 185 nm (Fig. 3b). The magnetic configuration therein comprises three skyrmionic vortices, with the longest one formed nearly parallel to the $[01\overline{1}]$ edge and the other two terminating at a side edge, as shown in the equi-spin surface presentation (Fig. 3f). The core magnetization of all three vortices points in the same [001] direction, whereas the spacing between vortices has magnetization mostly in the $[00\overline{1}]$ direction (Fig. 3e). The important discrete nature of these skyrmionic states further supports their topological nature. Even larger tetrahedral particles host the helimagnetic state, which is the ground state in bulk³⁰. As the particle size increases (Fig. 3c,d), there is also a transition of the helical wavevector (q) from along the <100> to the <111> direction. This transition is primarily driven by the competition between magnetocrystalline anisotropy and dipole-dipole interaction. Details of the energy analysis are given in Supplementary Note 3.

Role of chiral geometric frustration. The formation of a skyrmionic vortex is closely related to the edge spin twists and topological defects formed at the edge of a tetrahedron. These defect states are induced by the chiral geometric frustration originating from the interplay between the tetrahedral geometry and the chiral spin interactions. At surfaces and edges of any geometry, it is general that the symmetry of bulk spin interactions is broken because of missing neighbouring lattices sites and/or the presence of defects and irregular lattice sites^{33,42,43}. Taking the helimagnet plane shown in Fig. 4a as an example, the zero-field ground state is a helical state, and parallel helical stripes (black arrows) develop. Enabled by the DM interaction, the missing neighbours at the boundaries perpendicular to the helical stripes (here, the left and right boundaries) give rise to edge spin twists (indicated by the red arrows) in which spins point along

ARTICLES NATURE MATERIALS

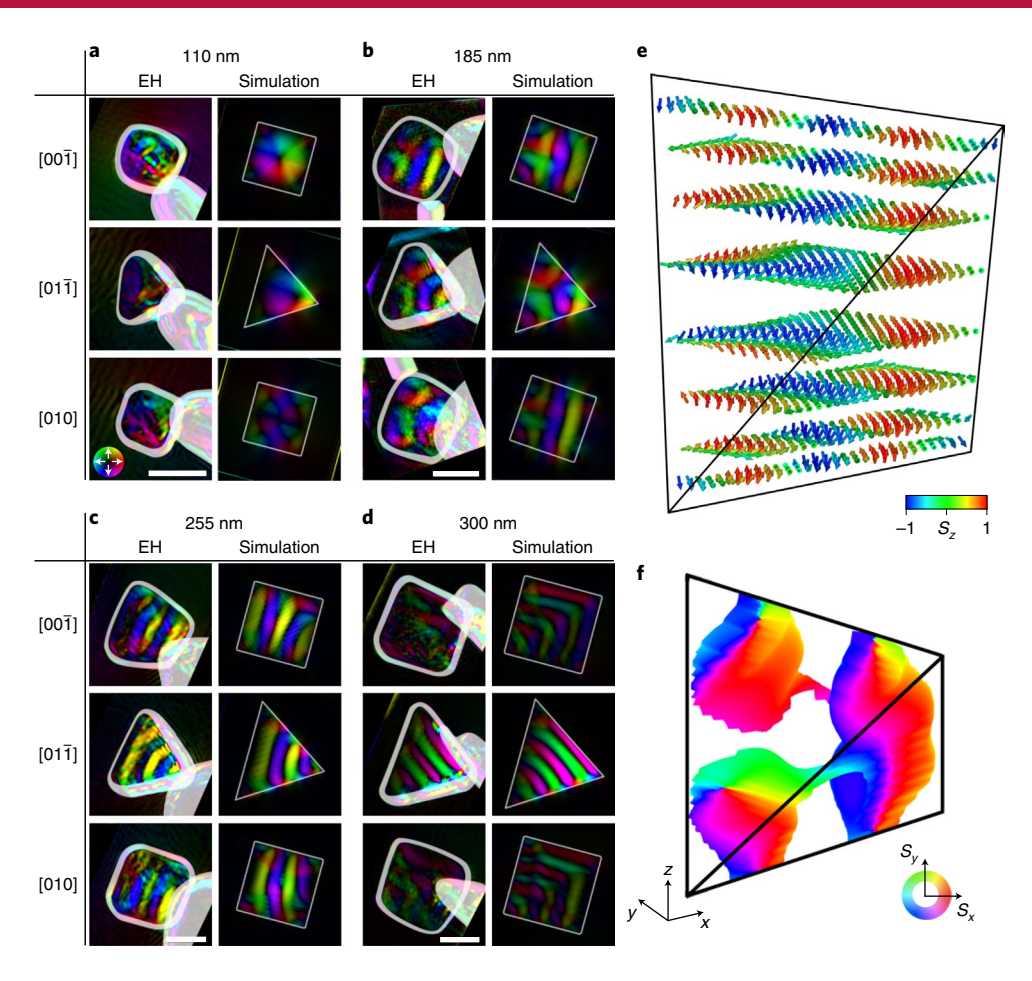


Fig. 3 | **Observed and simulated projections of non-trivial magnetic states. a**, A 110 nm particle hosting a skyrmionic vortex. **b**, A 185 nm particle hosting three skyrmionic vortices. **c**, A 255 nm particle hosting q = [100] helices. **d**, A 300 nm particle hosting q = [111] helices. **e**, **f**, Vector plot (**e**) and equi-spin surface (for $S_z = 0$) (**f**) of the three-skyrmionic vortices in a 185 nm tetrahedron. Scale bars, 100 nm.

the edge and close the magnetic flux of the adjacent helical strip. Such edge spin twists have already been observed experimentally in FeGe nanostripes^{26,27}. Once the plane is folded and a new edge is created (Fig. 4b), the helical stripes are broken into two parts, and geometrical frustration occurs; the left plane favours the edge twist indicated by the left dashed arrows, whereas the right plane favours the edge twist indicated by the right dashed arrows. Such geometric frustration of chiral origin, or 'chiral geometric frustration', gives rise to an unconventional type of edge spin twist, as shown in Fig. 4b (solid blue arrows and dot). Intrinsic chiral geometric frustration is a natural consequence for any edge in chiral magnets. For more details on the chiral geometric frustration and edge spin twist, see Supplementary Note 5.

For the geometry of a tetrahedron, each edge of the tetrahedron adjoins two lateral surfaces, thus the spins therein suffer from chiral geometric frustration. As shown in Fig. 4c, the top edge (red line) adjoins the (111) and (11 $\bar{1}$) facets of the tetrahedron. To compensate for spin twists from adjacent surfaces, half spins on the edge take one direction, and the other half take the opposite direction (Fig. 4c). Two counterpropagating spin twists meet at the midpoint of the edge, and a Néel-type domain wall emerges. In the (1 $\bar{1}$ 0) plane containing the bottom edge and midpoint of the top edge (Fig. 4d), the Néel-type domain wall, together with spins along the [00 $\bar{1}$] direction, resembles a fractional vortex on the bottom edge; the (110) plane (Fig. 4e) also hosts a fractional vortex on the top edge. Each fractional vortex carries a winding number of -1/2 in the plane. In contrast to the findings in previous studies the fractional vortices

formed here are mainly stabilized by the DM interaction rather than by the magnetic dipole–dipole interaction. Two fractional vortices are connected via a vertical line on which spins point in the $[00\overline{1}]$ direction. This line comprises the spine of the skyrmionic tube. This is the reason why the skyrmionic tube ends at two opposite edges. Hence the formation of skyrmionic vortices can be mainly attributed to chiral geometric frustration.

Indeed, we can capture the essential feature of the Néel-like edge spin twists that form various types of magnetic and topological orders. The lower panels of Supplementary Fig. 20 represent the simulated 3D spin configurations for $145\,\mathrm{nm}$, $255\,\mathrm{nm}$ and $300\,\mathrm{nm}$ tetrahedra forming two, four and three twisted edges, respectively (highlighted in magenta). These edges form a long-range order inside the particles, resulting in a skyrmionic vortex, [100] helices and $[11\bar{1}]$ helices. The projections of their simulated spatial magnetic configurations consistently reproduce these observations, corroborating the existence and novel role of chiral geometric frustration in tetrahedral particles.

Size and temperature dependence of stable magnetic states. Although the particle size range in which a single skyrmionic vortex emerges is quite limited, the robustness of this configuration in 0D is dramatically improved compared with that of skyrmions in 1D and 2D geometries^{29,30,36}.

Figure 5 shows a magnetic phase diagram as a function of temperature and particle size, together with a ground-state phase diagram as a function of particle size deduced from the

NATURE MATERIALS ARTICLES

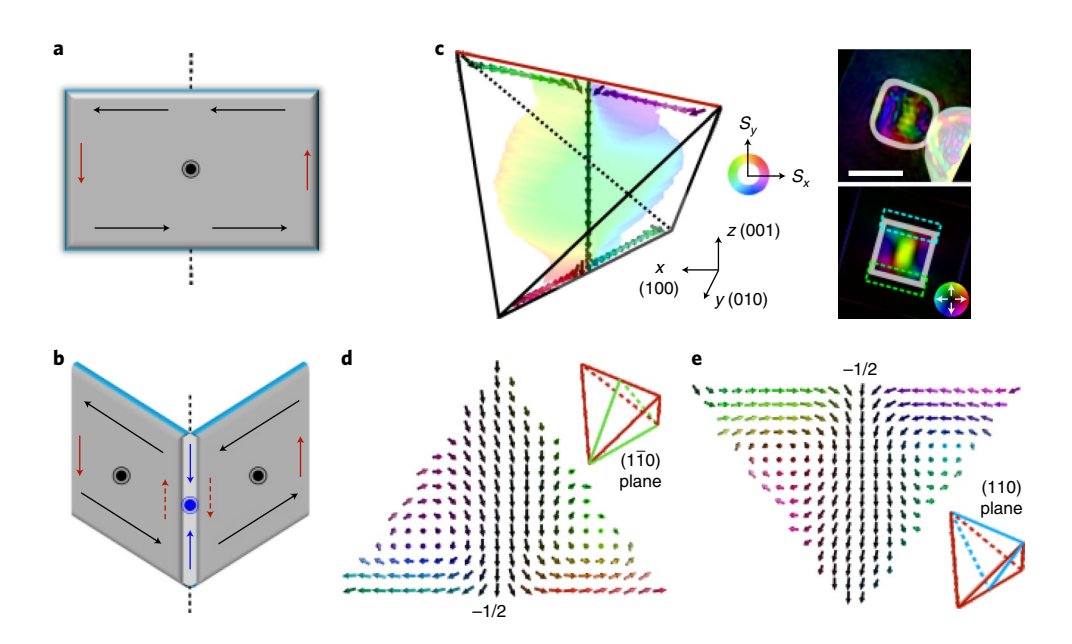


Fig. 4 | Chiral edge state in a tetrahedron. a,b, Schematics of the spin twists at the edge in an unfolded (**a**) and folded (**b**) chiral magnet thin film. A spin helix with its q vector along the y axis is sketched. The black arrows and dots represent the spins of the helical stripe; the red arrows represent the directions of spin twist at the boundary; the blue arrows represent Néel-like edge spin twists formed as a consequence of chiral geometric frustration; and the dashed red arrows represent the preferred spin directions at the boundary for the case without a connected folding edge. **c**, Left: Simulated edge spin twists with Néel-type domain walls at the top and bottom edges of a 145 nm tetrahedron. The formed skyrmionic vortex is shown as a light-coloured tube. Right: The corresponding observed (top) and simulated (bottom) projections of the skyrmionic vortex along the [001] direction. Rectangles drawn with a dashed line in the bottom indicate positions of the formed Néel-like edge spin twists. Scale bar, 100 nm. **d,e**, Detailed spin distributions on the $(1\overline{10})$ (**d**) and (110) (**e**) planes. Fractional vortices with a winding number of -1/2 emerge at the midpoints of the horizontal edges. For clarity, the chirality and polarity of the skyrmion shown here are opposite to those in Fig. 1.

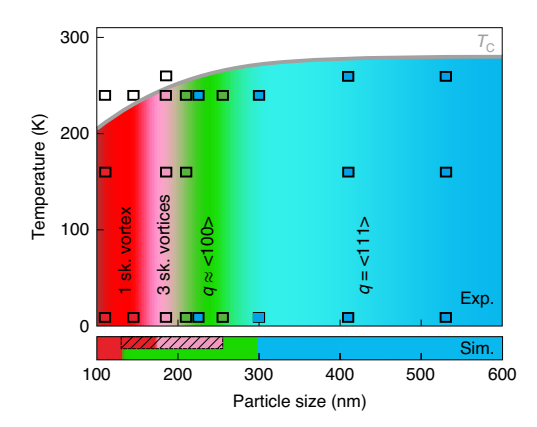


Fig. 5 | Magnetic phase diagram of the FeGe tetrahedral particle system. Each plot represents an experimental observation data point. The bottom row represents the ground state deduced from micromagnetic simulations; the hatched region represents metastable states. The areas labelled 1 sk. vortex, 3 sk. vortices, $q \approx <100>$ and q = <111> represent the single-skyrmionic-vortex state, the three-skyrmionic-vortex state and the helical state with propagating vector of $q \approx <100>$ and q = <111>, respectively. Exp., experiment; Sim., simulation.

micromagnetic simulations. Detailed observations are summarized in Supplementary Fig. 22 in a matrix of temperature and particle size. The q vectors of the observed helices are identified by comparison with the model-based imaging simulations of Supplementary Fig. 10. The critical temperature of magnetic orderings somewhat decreased as the particle size was reduced, presumably because of the increasing contribution from the

configurational instabilities near the surface. The simulated results for the ground state reproduce the essential trend of the observed results at $10\,\mathrm{K}$, although some observed magnetic states are predicted to be energetically metastable (see Supplementary Note 3 for details). The skyrmionic vortex state is relatively stable as the particle size decreases and eventually becomes the ground state below $130\,\mathrm{nm}$ in size, as inferred from the micromagnetic simulation results. Within this size range, this state is robust from the T_C down to a cryogenic temperature even in the absence of a magnetic field, indicating that the 0D chiral geometric frustration originating from the geometrical confinement plays a dominant role in stabilizing this topologically non-trivial magnetic configuration.

Outlook. We investigated the intriguing and diverse magnetic structures geometrically confined in tetrahedral particles of skyrmion-hosting FeGe using EH imaging and micromagnetic simulations. This integrated approach, which combines observed and simulated imaging for multiple projection angles, revealed that the zero-dimensional confinement stabilizes an unconventional skyrmionic vortex state. Unlike the conventional skyrmion, the skyrmionic vortex emerges as a consequence of chiral geometric frustration, wherein a Néel-like rotation with a narrower pitch is emergent near the two opposing edges, whereas a Bloch-like rotation with a wider pitch is present in the central cross section. The resultant potbelly-shaped equi-spin surface reflects the particle nature. The skyrmionic vortex exhibits dramatically improved robustness throughout the temperature range below T_C without the application of any stimuli, such as magnetic or electric fields. These results shed light on the unexplored role of 0D confinement on diverse magnetic and topological orders. This confinement in combination with other geometrical effects (for example, curvature effects⁴⁴) can offer a novel way to manipulate any desired number of ARTICLES NATURE MATERIALS

skyrmionic vortices, thus providing a promising platform for skyrmionic engineering.

Online content

Any methods, additional references, Nature Research reporting summaries, source data, extended data, supplementary information, acknowledgements, peer review information; details of author contributions and competing interests; and statements of data and code availability are available at https://doi.org/10.1038/s41563-021-01186-x.

Received: 8 March 2021; Accepted: 6 December 2021; Published online: 27 January 2022

References

- Allwood, D. A. et al. Magnetic domain-wall logic. Science 309, 1688–1692 (2005).
- Parkin, S. S., Hayashi, M. & Thomas, L. Magnetic domain-wall racetrack memory. Science 320, 190–194 (2008).
- Wolf, D., Lubk, A., Röder, F. & Lichte, H. Electron holographic tomography. Curr. Opin. Solid State Mater. Sci. 17, 126–134 (2013).
- Wolf, D. et al. 3D magnetic induction maps of nanoscale materials revealed by electron holographic tomography. Chem. Mater. 27, 6771–6778 (2015).
- Wolf, D. et al. Holographic vector field electron tomography of three-dimensional nanomagnets. Commun. Phys. 2, 87 (2019).
- Hilger, A. et al. Tensorial neutron tomography of three-dimensional magnetic vector fields in bulk materials. *Nat. Commun.* 9, 4023 (2018).
- Donnelly, C. et al. Three-dimensional magnetization structures revealed with X-ray vector nanotomography. *Nature* 547, 328–331 (2017).
- Donnelly, C. et al. Tomographic reconstruction of a three-dimensional magnetization vector field. New J. Phys. 20, 083009 (2018).
- Phatak, C., Petford-Long, A. K. & De Graef, M. Three-dimensional study of the vector potential of magnetic structures. *Phys. Rev. Lett.* 104, 253901 (2010).
- 10. Tanigaki, T. et al. Three-dimensional observation of magnetic vortex cores in stacked ferromagnetic discs. *Nano Lett.* **15**, 1309–1314 (2015).
- 11. Streubel, R. et al. Retrieving spin textures on curved magnetic thin films with full-field soft X-ray microscopies. *Nat. Commun.* **6**, 7612 (2015).
- Lai, G. et al. Three-dimensional reconstruction of magnetic vector fields using electron-holographic interferometry. J. Appl. Phys. 75, 4593–4598 (1994).
- 13. Gubin, S. P. Magnetic Nanoparticles (Wiley-VCH, 2009).
- Mühlbauer, S. et al. Magnetic small-angle neutron scattering. Rev. Mod. Phys. 91, 015004 (2019).
- 15. Skyrme, T. H. R. A unified field theory of mesons and baryons. *Nucl. Phys.* 31, 556–569 (1962).
- 16. Mühlbauer, S. et al. Skyrmion lattice in a chiral magnet. *Science* **323**, 915–919 (2009).
- 17. Yu, X. Z. et al. Real-space observation of a two-dimensional skyrmion crystal. *Nature* **465**, 901–904 (2010).
- Jonietz, F. et al. Spin transfer torques in MnSi at ultralow current densities. Science 330, 1648–1651 (2010).
- Nagaosa, N. & Tokura, Y. Topological properties and dynamics of magnetic skyrmions. Nat. Nanotechnol. 8, 899–911 (2013).
- Fert, A., Cros, V. & Sampaio, J. Skyrmions on the track. Nat. Nanotechnol. 8, 152–156 (2013).
- Parkin, S. & Yang, S. H. Memory on the racetrack. *Nat. Nanotechnol.* 10, 195–198 (2015).

- Liang, D., DeGrave, J. P., Stolt, M. J., Tokura, Y. & Jin, S. Current-driven dynamics of skyrmions stabilized in MnSi nanowires revealed by topological Hall effect. *Nat. Commun.* 6, 8217 (2015).
- Fert, A., Reyren, N. & Cros, V. Magnetic skyrmions: advances in physics and potential applications. *Nat. Rev. Mater.* 2, 17031 (2017).
- Sampaio, J., Cros, V., Rohart, S., Thiaville, A. & Fert, A. Nucleation, stability and current-induced motion of isolated magnetic skyrmions in nanostructures. *Nat. Nanotechnol.* 8, 839–844 (2013).
- Jiang, W. et al. Magnetism. Blowing magnetic skyrmion bubbles. Science 349, 283–286 (2015).
- Du, H. et al. Edge-mediated skyrmion chain and its collective dynamics in a confined geometry. Nat. Commun. 6, 8504 (2015).
- Jin, C. et al. Control of morphology and formation of highly geometrically confined magnetic skyrmions. Nat. Commun. 8, 15569 (2017).
- Iwasaki, J., Mochizuki, M. & Nagaosa, N. Current-induced skyrmion dynamics in constricted geometries. Nat. Nanotechnol. 8, 742–747 (2013).
- Mathur, N., Stolt, M. J. & Jin, S. Magnetic skyrmions in nanostructures of non-centrosymmetric materials. APL Mater. 7, 120703 (2019).
- Yu, X. Z. et al. Near room-temperature formation of a skyrmion crystal in thin-films of the helimagnet FeGe. Nat. Mater. 10, 106–109 (2011).
- Zhao, X. et al. Direct imaging of magnetic field-driven transitions of skyrmion cluster states in FeGe nanodisks. *Proc. Natl Acad. Sci. USA* 113, 4918–4923 (2016).
- 32. Matsumoto, T., So, Y. G., Kohno, Y., Ikuhara, Y. & Shibata, N. Stable magnetic skyrmion states at room temperature confined to corrals of artificial surface pits fabricated by a focused electron beam. *Nano Lett.* 18, 754–762 (2018).
- Rohart, S. & Thiaville, A. Skyrmion confinement in ultrathin film nanostructures in the presence of Dzyaloshinskii–Moriya interaction. *Phys. Rev. B* 88, 184422 (2013).
- Beg, M. et al. Ground state search, hysteretic behaviour, and reversal mechanism of skyrmionic textures in confined helimagnetic nanostructures. Sci. Rep. 5, 17137 (2015).
- 35. Zheng, F. et al. Direct imaging of a zero-field target skyrmion and its polarity switch in a chiral magnetic nanodisk. *Phys. Rev. Lett.* **119**, 197205 (2017).
- Stolt, M. J. et al. Selective chemical vapor deposition growth of cubic FeGe nanowires that support stabilized magnetic skyrmions. *Nano Lett.* 17, 508–514 (2017)
- Hou, Z. et al. Creation of single chain of nanoscale skyrmion bubbles with record-high temperature stability in a geometrically confined nanostripe. *Nano Lett.* 18, 1274–1279 (2018).
- Moon, K. et al. Spontaneous interlayer coherence in double-layer quantum Hall systems: charged vortices and Kosterlitz-Thouless phase transitions. *Phys. Rev. B* 51, 5138-5170 (1995).
- 39. Rybakov, F., Borisov, A. & Bogdanov, A. Three-dimensional skyrmion states in thin films of cubic helimagnets. *Phys. Rev. B* **87**, 094424 (2013).
- Tchernyshyov, O. & Chern, G. W. Fractional vortices and composite domain walls in flat nanomagnets. *Phys. Rev. Lett.* 95, 197204 (2005).
- 41. Almeida, T. P. et al. Direct visualization of the thermomagnetic behavior of pseudo-single-domain magnetite particles. *Sci. Adv.* 2, e1501801 (2016).
- Bogdanov, A. N. & Rössler, U. K. Chiral symmetry breaking in magnetic thin films and multilayers. *Phys. Rev. Lett.* 87, 037203 (2001).
- 43. Cubukcu, M. et al. Dzyaloshinskii–Moriya anisotropy in nanomagnets with in-plane magnetization. *Phys. Rev. B* **93**, 020401 (2016).
- 44. Volkov, M. O. et al. Mesoscale Dzyaloshinskii–Moriya interaction: geometrical tailoring of the magnetochirality. *Sci. Rep.* **8**, 866 (2018).

Publisher's note Springer Nature remains neutral with regard to jurisdictional claims in published maps and institutional affiliations.

© The Author(s), under exclusive licence to Springer Nature Limited 2022

NATURE MATERIALS ARTICLES

Methods

Sample preparation. Nanostructures of FeGe structural polymorphs with a 1:1 Fe/Ge composition were synthesized using a chemical vapour deposition method where the growth zone temperature of the reaction was set to 500–600 °C following a previously reported procedure³⁶. Highly symmetric tetrahedral particles of various sizes (Fig. 1a, right column) were picked up on sharpened tungsten needles, and the needles were installed onto a lift-out grid (Fig. 2a). Particles greater than 300 nm in size were directly dispersed onto a lacey carbon grid and used for EH observations.

Electron holography. Electron holograms were formed by double-biprism interferometry45 and recorded by a charge-coupled device camera (UltraScan4000, GATAN) with a 300 kV TEM (HF-3300S, Hitachi). The EH observation angles and temperatures were coordinated using a double-tilt liquid-helium cooling holder (ULTDT, GATAN). The maximum tilt angle β was ±18°. The mechanical configuration for the EH observation is illustrated in Supplementary Fig. 1. As the opening angle without any mechanical interference was $50^{\circ} \pm 2^{\circ}$ (Supplementary Fig. 1), three systematic tilts through the [010], $[01\overline{1}]$ and $[00\overline{1}]$ directions were feasible only by rotating the α tilt, which is 360° rotatable and employed on the TEM goniometer, when the initial sample loading at $\alpha = 0^{\circ}$ would satisfy nearly $[01\overline{1}]$ projection, as illustrated in Supplementary Fig. 1. The exact tilt angles of the crystallographic orientations were preliminarily checked by nanobeam electron diffraction (Fig. 1l-n). The angle misalignment with temperature was within a solid angle of \sim 2°. We performed liquid helium transfer and consumed almost half of the filled liquid helium for cooling the sample and capillaries at $\alpha = 0^{\circ}$. The holder was then gradually tilted to $\alpha \approx \pm 45^{\circ}$ to avoid exceeding the internal pressure resistance of the liquid helium Dewar. Our set-up allowed the lowest settled temperature of 10 K to be maintained for ~80 min with $\alpha \approx \pm 45^{\circ}$. When the Dewar was empty, it was refilled with liquid helium after restoring the tilts.

For hologram acquisition, the sample was slightly tilted away from the exact crystallographic (010), (011) and (001) planes to escape strong diffraction contrasts. During the heating sequence from 10 K, batches of multiple (>20) holograms were recorded for the aimed projections at several settled temperatures of 10, 160, 240, 260 and 293 K. Each batch of holograms was reconstructed into that of the phase images and averaged into one phase image after drift compensation. To subtract the phase shift due to the mean inner potential, the averaged phase image at 293 K was subtracted from those below the magnetic ordering temperature ($T_{\rm C}$) (that is, 10, 160, 240 and 260 K). A typical dataset of this protocol is provided in Supplementary Fig. 2. The fringe contrast and pitch were 18.9% and 5.5 nm, respectively. The resultant spatial and phase resolutions of the averaged reconstructed phase images were approximated to be 12.5 nm and 0.05 rad, respectively.

In the phase reconstruction and subtraction processes, unwanted artefacts that could disturb the projections of in-plane magnetic fluxes were superposed onto the reconstructed phase images. Their origins and significance are described in Supplementary Note 2. Areas suffering from these artefacts were masked with a transparent white colour.

Model-based imaging simulations. Model-based imaging simulations were performed using the commercial ELF-MAGIC code. This code enabled the projection component (A_{pj}) of magnetic vector potentials **A** both inside and outside of the modelled magnetic building blocks to be calculated and integrated along the aimed projection direction. The A_{pj} distributions were calculated with respect to the [010], $[01\overline{1}]$ and $[00\overline{1}]$ projections.

The relation between the magnetic phase shift $(\Delta \varphi)$ and the magnetic flux B normal to the projection direction (that is, in-plane: B_n) is given by

$$\Delta \varphi = \frac{\mathrm{e}}{h/2\pi} \iint B_{\mathrm{n}} \mathrm{d}S$$

and from Stokes's theorem, we have

$$\oint \mathbf{A} \cdot d\mathbf{s} = \iint \text{rot} \mathbf{A} \cdot d\mathbf{S} = \iint B_{n} dS$$

Therefore, we can derive the integrated in-plane magnetic flux $B_{\rm n}$ from the integrated $A_{\rm pj}$ and from $\Delta \varphi$ (ref. ⁴⁶). The $B_{\rm n}$ distribution was displayed with colour coding, where the colour hue and brightness represent the direction and density, respectively. For simplicity, the electrostatic potential of the blocks was set to zero. The protocol is schematically presented in Supplementary Fig. 8.

Micromagnetic simulations. To investigate the magnetic ground state of B20-type FeGe tetrahedral particles, micromagnetic simulations were performed using the open-source software package MuMax3⁴⁷. Material parameters were employed in the simulations with a saturation magnetization M_s = 384 kA m⁻¹, a spin-wave

exchange stiffness constant $A = 4.75 \,\mathrm{pJ}\,\mathrm{m}^{-1}$, a bulk-type DM interaction strength $D = 0.8527 \,\mathrm{mJ}\,\mathrm{m}^{-2}$, a first-order cubic anisotropy $K_c = -6 \,\mathrm{kJ}\,\mathrm{m}^{-3}$ and a second-order cubic anisotropy $K_{c2} = 12 \text{ kJ m}^{-3}$. The sign of DM interaction was positive for the 110 nm tetrahedron and negative for the 145 nm and 185 nm tetrahedra, reflecting the crystallographic handedness of the respective nanoparticle; it is expected to be random or stochastic from particle to particle because the left- and right-handednesses are energetically degenerated^{48,49}. The magnetic dipole—dipole interaction was taken into account to incorporate the effect of the tetrahedral shape. Particles ranging in size from 100 to $600\,\mathrm{nm}$ were constructed with $3\,\mathrm{nm}$ \times 3 nm \times 3 nm cubic cells. The surface anisotropy (uniaxial type with the axial direction normal to each surface) was also considered. Several ansatz were used for the initial spin textures: a random state, a single skyrmion state, a two-skyrmion state, a three-skyrmion state, a uniform state (with the spin direction along the z axis), a helical state along the [001] direction and a helical state along the [111] direction. After energy minimization using the conjugate gradient method, the energies of different states were compared to determine the ground state. To accurately reproduce the EH phase images, for the 145 nm tetrahedron, a surface anisotropy (easy-plane type) $K_s = 95 \,\mu\text{J m}^{-2}$ was used, and for the 185 nm tetrahedron, a reduced saturation magnetization $M_{\rm S}$ = 192 kA m⁻¹ was employed. The simulated results were then input into the model-based imaging simulations and converted into the in-plane magnetic flux distributions along the [010], $\lceil 01\overline{1} \rceil$ and $\lceil 00\overline{1} \rceil$ directions to facilitate comparison with the experimental EH observations. The protocol is shown in Supplementary Fig. 9.

Data availability

The data that support the findings of this study are available within the article and its Supplementary Information. Any other relevant data are also available upon reasonable request from the corresponding authors.

References

- Harada, K., Tonomura, A., Togawa, Y., Akashi, T. & Matsuda, T. Double-biprism electron interferometry. *Appl. Phys. Lett.* 84, 3229–3231 (2004).
- Shindo, D. & Murakami, Y. Electron holography of magnetic materials. J. Phys. D 41, 183002 (2008).
- Vansteenkiste, A. et al. The design and verification of MuMax3. AIP Adv. 4, 107133 (2014).
- Dyadkin, V. A. et al. Control of chirality of transition-metal monosilicides by the Czochralski method. *Phys. Rev. B* 84, 014435 (2011).
- 49. Morikawa, D. et al. Determination of crystallographic chirality of MnSi thin film grown on Si(111) substrate. *Phys. Rev. Mater.* 4, 014407 (2020).

Acknowledgements

K.N. was supported by a Grant-in-Aid for Scientific Research (B) (number 19H02418) and for Challenging Research (Exploratory) (number 19K22052) from the JSPS. X.Y. was supported by a Grant-in-Aid for Scientific Research (A) (number 19H00660) from the JSPS and JST CREST (grant number JPMJCR20T1). N.N. was supported by JST CREST (grant number JPMJCR1874). A.C.B. and J.Z. acknowledge support from the US Department of Energy (DOE), Office of Science, Basic Energy Sciences (BES) under award number DE-SC0020221. Y.L. was supported by the Special Postdoctoral Researcher programme of RIKEN. N.M., M.J.S. and S.J. were supported by US NSF grant ECCS-1609585. M.J.S. also acknowledges support from the NSF Graduate Research Fellowship Program.

Author contributions

S.J. and Y.T. conceived the project. N.M., M.J.S. and S.J. synthesized the FeGe particles. Y.L., A.C.B. and J.Z. performed the micromagnetic simulations. K.N. performed the EH observations and model-based simulations. K.N., Y.L. and J.Z. wrote the manuscript. All authors discussed the data and revised the manuscript.

Competing interests

The authors declare no competing interests.

Additional information

Supplementary information The online version contains supplementary material available at https://doi.org/10.1038/s41563-021-01186-x.

Correspondence and requests for materials should be addressed to Kodai Niitsu or Jiadong Zang.

Peer review information Nature Materials thanks Shawn D. Pollard and the other, anonymous, reviewer(s) for their contribution to the peer review of this work.

Reprints and permissions information is available at www.nature.com/reprints.